Virus Evolution, 2024, **10(1)**, veae055
DOI: https://doi.org/10.1093/ve/veae055
Advance Access Publication 16 July 2024
Research Article

Adaptation of turnip mosaic virus to *Arabidopsis thaliana* involves rewiring of VPg–host proteome interactions

José L. Carrasco[1], Silvia Ambrós[1], Pablo A. Gutiérrez[2], Santiago F. Elena[1,3,*]

[1]Instituto de Biología Integrativa de Sistemas (CSIC—Universitat de València), Catedratico Agustin Escardino 9, Paterna, València 46182, Spain
[2]Laboratorio de Microbiología Industrial, Facultad de Ciencias, Universidad Nacional de Colombia, Carrera 65 Nro. 59A - 110, Medellín, Antioquia 050034, Colombia
[3]The Santa Fe Institute, 1399 Hyde Park Rd, Santa Fe, NM 87501, United States

*Corresponding author. The Santa Fe Institute, 1399 Hyde Park Rd, Santa Fe, NM 87501, United States. E-mail: santiago.elena@csic.es

Abstract

The outcome of a viral infection depends on a complex interplay between the host physiology and the virus, mediated through numerous protein–protein interactions. In a previous study, we used high-throughput yeast two-hybrid (HT-Y2H) to identify proteins in *Arabidopsis thaliana* that bind to the proteins encoded by the turnip mosaic virus (TuMV) genome. Furthermore, after experimental evolution of TuMV lineages in plants with mutations in defense-related or proviral genes, most mutations observed in the evolved viruses affected the VPg cistron. Among these mutations, D113G was a convergent mutation selected in many lineages across different plant genotypes, including *cpr5-2* with constitutive expression of systemic acquired resistance. In contrast, mutation R118H specifically emerged in the *jin1* mutant with affected jasmonate signaling. Using the HT-Y2H system, we analyzed the impact of these two mutations on VPg's interaction with plant proteins. Interestingly, both mutations severely compromised the interaction of VPg with the translation initiation factor eIF(iso)4E, a crucial interactor for potyvirus infection. Moreover, mutation D113G, but not R118H, adversely affected the interaction with RHD1, a zinc-finger homeodomain transcription factor involved in regulating DNA demethylation. Our results suggest that RHD1 enhances plant tolerance to TuMV infection. We also discuss our findings in a broad virus evolution context.

Keywords: experimental evolution; protein–protein interactions; targets of adaptation; virus evolution.

1. Introduction

Viruses establish multiple contact points with the host proteome, primarily through a limited number of proteins, particularly reduced in the case of RNA viruses (Belshaw et al. 2007, Mahmoudabadi and Phillips 2018). This interaction involves virus–host protein–protein interactions (PPIs) that result in the manipulation of various cellular pathways for creating favorable replication conditions. This manipulation can occur by sequestering cell resources for the virus's benefit or by interfering with immune responses. Simultaneously, host cell receptors play a role in sensing foreign elements and responding accordingly. Recent years have seen significant progress in creating detailed, high-quality maps of virus-host PPIs (Uetz et al. 2006, De Chassey et al. 2008). Integrative approaches have identified both general and specific molecular mechanisms employed by different viruses (Dyer et al. 2008, Mukhtar et al. 2011, Pichlmair et al. 2012, Ahmed et al. 2018, Aguirre and Guantes 2023). These findings, coupled with additional omics data, have been used to predict phenotypic outcomes of infection (Tisoncik-Go et al. 2016, Cervera et al. 2018, Tarazona et al. 2020). These advancements build upon the continuous development of a comprehensive large-scale map of host PPIs, which, while not fully complete, proves valuable in recognizing disease-associated modules (Mukhtar et al. 2011, Menche et al. 2015).

In a previous study, Martínez et al. (2023) systematically identified direct PPIs between turnip mosaic virus strain YC5 (TuMV; species *Turnip mosaic virus*, genus *Potyvirus*, family *Potyviridae*) and its hosts, *Arabidopsis thaliana* (L.) Heynh, using high-throughput yeast two-hybrid (HT-Y2H) screenings. This study uncovered 378 new PPIs between TuMV and plant proteomes. Among the viral proteins, the RNA-dependent RNA polymerase NIb emerged with the highest number of contacts, including crucial salicylic acid (SA)-dependent transcription regulators. The authors constructed and analyzed a network consisting of 399 TuMV-*A. thaliana* interactions, incorporating intravirus and intrahost connections. Notably, their findings revealed that TuMV-targeted host proteins (i) were enriched in various aspects of plant responses to infections, (ii) exhibit greater connectivity, (iii) had enhanced capacity to disseminate information throughout the cell proteome, (iv) showed higher expression levels, and (v) were under stronger purifying selection than expected by chance.

In previous evolution experiments with potyviruses, the VPg cistron has been identified as a significant target of selection. For instance, Agudelo-Romero et al. (2008a) observed that a single amino acid replacement in VPg significantly increased tobacco etch virus (TEV) infectivity, severity of symptoms, and viral load in *A. thaliana*. Later on, Hillung et al. (2014) further described additional VPg mutants in several *A. thaliana* ecotypes that differed in their susceptibility to TEV infection. Likewise, Navarro et al. (2022) and Ambrós et al. (2024) evolved TuMV lineages in different defense-deficient genotypes of *A. thaliana*, observing pervasive mutations affecting VPg, with remarkable examples of parallel evolution with the same mutations fixing in lineages evolved in the same host genotype. Gallois et al. (2010) found that *A. thaliana* plants with knock-out mutations in the *EUKARYOTIC TRANSLATION INITIATION FACTORS (ISO)4E, (ISO)4 G1* and *(ISO)4 G2* [*eIF(iso)4E, eIF(iso)4 G1* and *eIF(iso)4 G2*, respectively] genes were resistant to TuMV infection, demonstrating the proviral role of these eIFs. However, two mutations in VPg were sufficient to overcome this resistance and revert to the original infection phenotype. Notably, Y2H assays showed that these mutations did not preclude the binding of VPg to eIF(iso)4E (Gallois et al. 2010). As another example, the *pvr2* locus, one of the most extensively used resistance genes against potato virus Y (PVY) in pepper cultivars, encodes the eIF4E factor, which physically interacts with VPg. Interestingly, all resistance-breaking viral isolates identified so far contain mutations in the VPg cistron (Duprat et al. 2002, Moury et al. 2004, Ayme et al. 2006).

VPg has been described as a scaffolding protein that interacts with other potyviral proteins (Bosque et al. 2014, Hafrén et al. 2015) and with many host proteins (Martínez et al. 2016, 2023), most notably factors involved in genome transcription, being linked to the 5′-end of the viral genome and providing the hydroxyl group that primes the synthesis of complementary strands by the viral NIb replicase (Eskelin et al. 2011). Additionally, it plays a role in protein synthesis by directly interacting with canonical translation factors eIF(iso)4E and eIF(iso)4 G (Gallois et al. 2010, Hafrén et al. 2015) and with the antiviral factor eIF4E1 that protects the translational machinery during TuMV infection (Zafirov et al. 2023). Indeed, Martínez et al.'s (2023) HT-Y2H analyses and literature curation resulted in the identification of 43 direct interactors, involved in diverse cellular processes. Amongst the most highly expressed and connected genes, *CALNEXIN 1* (*CNX1*) and *OBERON 1* (*OBE1*) were shown to directly interact with VPg. Both CNX1 and OBE1 proteins were proviral factors whose knocked-out expression resulted in late and less severe symptoms Other genes such as *NONEXPRESSER OF PATHOGENESIS-RELATED GENES 1* (*NPR1*), *SUMO 3* (*SUM3*), *SUMO CONJUGATING ENZYME 1* (*SCE1*), and specially *TGACG SEQUENCE-SPECIFIC BINDING FACTOR 1* (*TGA1*) also resulted in milder disease symptoms, although their interaction with VPg was mediated by NIb.

In various evolution experiments of TuMV isolate YC5 in different *A. thaliana* genotypes, it has consistently been observed that VPg fixed nonsynonymous mutations; 14 identified as being subject to positive selection (González et al. 2019, 2021, Navarro et al. 2022, Melero et al. 2023, Ambrós et al. 2024). The majority of these positively selected mutations are concentrated within a helix-coil-helix structural domain, spanning amino acids 110–120 [Fig. 4b in Ambrós et al. (2024)]. Certain mutations were consistently present across lineages that evolved in different host genotypes and environmental conditions. For instance, the VPg^{D113G} mutation was observed in lineages evolved in nine plant genotypes and two environmental conditions, including wild-type Col-0 plants (González et al. 2019, 2021, Navarro et al. 2022, Ambrós et al. 2024) and *cpr5-2* (Navarro et al. 2022), a mutant of *CONSTITUTIVE EXPRESSOR OF PR GENES 5* that shows constitutive systemic acquired resistance (SAR) and strong resistance to infection. Conversely, some mutations were specific to particular host genotypes, such as the VPg^{R118H} mutation, found exclusively in lineages evolved in mutants of *JASMONATE INSENSITIVE 1* (*JIN1*) and *DECREASED DNA METHYLATION 1* (*DDM1*) genes, both being particularly permissive to TuMV infection (Navarro et al. 2022, Ambrós et al. 2024).

Given the prominent role played by VPg during potyvirus infections, its apparent prominence as target of natural selection and its promiscuous interaction with other potyviral and host proteins, a question that immediately arises from all previously mentioned studies is the extent to which these mutations affect the ability of VPg to engage into PPIs resulting in fitness increases. To tackle this question, we have selected mutants VPg^{D113G} and VPg^{R118H} as examples of what can be considered generalist and specialist versions of VPg, respectively. The two VPg mutants were cloned and used as bait proteins in HT-Y2H experiments to identify host interactors that differ from those obtained for VPg^{wt} by Martínez et al. (2023). Then, the relative affinity of the differential interactors was evaluated by a quantitative assay and compared with the VPg^{wt}. To further characterize the effect of these mutations in TuMV performance, we developed the corresponding infectious clones to inoculate *eif(iso)4e* and *ros1-associated homeodomain protein 1* (*rhd1*) mutant plants and characterized disease progression and viral accumulation. Finally, we performed *in silico* evaluations of the effect of the two mutations of interest in VPg folding and used docking and molecular dynamics techniques to evaluate their effect on the interaction with eIF(iso)4E and RHD1.

2. Materials and methods

2.1. Plasmid construction

TuMV infectious clones carrying the VPg mutations A6238G (D113G) or G6253A (R118H) were obtained by site-directed mutagenesis inverse PCR on the wild-type clone p35S-TuMV-YC5 (Chen et al. 2003) by using the QuikChange II XL Site-Directed Mutagenesis Kit (Agilent, Santa Clara, CA, USA) and the following primers set: VPg cpr5-2 F (5′-GGAGGATGAGTTGGgTCCAAATGAAATACGTGT-3′) plus VPg cpr5-2 R (5′-ACACGTATTTCATTTGGAcCCAACTCATCCTCC-3′) to obtain the VPg A6238G (D113G) mutant, and VPg jin1-F (5′- GGATCCAAATGAAATACaTGTGAATAAGACAATTC-3′) plus VPg jin1-R (5′-GAATTGTCTTATTCACAtGTATTTCATTTGGATCC-3′) to obtain the VPg G6253A (R118H) mutant. Bases in lowercase denote the specific point mutation. Inverse PCR reactions were performed according to the manufacturer's instructions and the following PCR profile: an initial denaturation step of 95°C ×2 min, 20 cycles of 95°C ×20 s, 60°C ×10 min and 68°C ×7 min, and a final extension step of 68°C ×5 min. Reactions were then incubated for 10 min with *Dpn*I and an aliquot of 1 μL was used to transform *Escherichia coli* One Shot TOP10 electrocompetent cells (ThermoFisher Scientific, Waltham, MA, USA). Plasmids from positive selected clones were sequenced on both strands (Sanger) in order to confirm the introduced mutations.

The mutated variants of the VPg cistron were then amplified by PCR from the above-mentioned clones using Phusion High-Fidelity DNA polymerase (ThermoFisher Scientific) according to manufacturer's recommendations and using primers specifically designed for the In-Fusion cloning system (Takara Bio, Mountain View, CA, USA). The amplified PCR fragments were recombined into the yeast bait two-hybrid vector pGBKT7 (Takara Bio, Kusatsu,

Japan), previously digested with *Eco*RI and *Bam*HI, using the In-Fusion enzyme. Thus, translational fusions of all three VPg protein variants (bait protein) with the GAL4 DNA-binding domain were generated.

2.2. High-throughput yeast two-hybrid screening

To search for differential interactors among the original VPg protein and the two selected mutated variants, an *A. thaliana* Col-0 cDNA library (Takara Bio) transformed into the *Saccharomyces cerevisiae* Y187 strain (prey strain) was screened using the Matchmaker® Gold Yeast Two-Hybrid System (Takara Bio). For that purpose, the three bait VPg proteins cloned in pGBKT7 were transformed in the yeast strain Y2HGold. Then, the Y187 prey strain was mated to each of the Y2HGold haploid bait strains expressing the wild-type and the mutated variants of VPg protein and plated on a double dropout medium (SD/-Leu/-Trp) containing 40 μg/mL X-α-Gal and 200 ng/mL aureobasidin A. Co-transformants displaying α-galactosidase activity were subjected to a second round of selection on a quadruple dropout medium (SD/-Leu/-Trp/-Ade/-His) also containing X-α-Gal. Plasmids pGBKT7-T-antigen, pGADT7-laminin C, and pGADT7-murine p53 (Takara Bio) were used as negative controls. cDNA inserts from positive yeast clones were amplified by colony PCR, digested with *Alu*I and analyzed by agarose gel electrophoresis to eliminate duplicate clones. Selected prey plasmids were rescued using a glass-bead extraction protocol and transformed into *Escherichia coli* DH5α for amplification and sequencing. DNA and protein sequence analyses were performed with the WU-BLAST algorithm. For each positive interaction, the prey plasmid was re-transformed into the yeast strain Y2HGold and mated to all three bait strains and also to a control Y187 yeast strain transformed with the empty pGBKT7 vector to remove false positives.

For the quantification of α-galactosidase, the procedure described in the Clontech Yeast Protocols Handbook (Takara Bio) was followed in a microtiter plate scale. Briefly, after measuring its OD_{600}, the supernatant of an overnight culture was incubated at 30°C with *p*-nitrophenyl-α-D-galactoside in an appropriate reaction buffer. Hydrolysis of this compound by α-galactosidase releases *p*-nitrophenol, which can be detected by measuring absorbance at 410 nm. The concentration of α-galactosidase was then measured using as:

$$\text{α-galactosidase (milliunits mL}^{-1}\text{ cell}^{-1}) = 1000 \times OD_{410} \times V_f/(\varepsilon \times b \times t \times V_i \times OD_{600})$$

where V_f is the final volume of the assay, ε is the *p*-nitrophenol molar absorption coefficient at 410 nm, b is the light path length, t is the time of incubation, and V_i the volume of culture supernatant added to the reaction.

2.3. Yeast protein extraction and Western-blot

Yeast strains were grown in selective medium at 30°C until reaching an OD_{600} of 0.5-0.6. Yeast cells were collected by centrifugation at 1000 g for 5 min and resuspended in 0.1 mL per 7.5 OD_{600} units of cracking buffer (40 mM Tris-HCl pH 6.8, 8 meter urea, 0.1 mM EDTA, 5% (w/v) SDS), supplemented with Halt™ Protease Inhibitor Cocktail (ThermoFisher Scientific). After adding a roughly similar volume of glass beads, cell suspensions were incubated at 70°C for 10 min and vortexed vigorously for 2 min. Extracts were clarified by centrifugation at 18 000 g and 4°C for 10 min, and stored at –80°C.

For Western-blot analysis, a monoclonal antibody against the GAL4 DNA-binding domain (Takara Bio) and a horseradish peroxidase-conjugated goat anti-mouse IgG (Active Motif, Carlsbad, CA, USA) were used following manufacturer's recommendations. HRP was detected by generating a chemiluminescence signal using the ECL™ Prime Western Blotting Detection Reagent (GE Healthcare, Buckinghamshire, UK), captured with an ImageQuant™ LAS 500 imager system (GE Healthcare).

2.4. Plant genotypes, virus clones, and inoculation procedures

Wild-type (WT) and two *A. thaliana* mutants were used in this study, all in the same Col-0 background. Seeds of the T-DNA insertion line SALK_092897C (*rhd1-1* mutant) were obtained from the Nottingham Arabidopsis Stock Center (NASC), whereas *eif(iso)4e* seeds were a kind gift from Dr Jean-Luc Gallois (INRA, Avignon, France) (Duprat et al. 2002).

TuMV infectious sap was obtained from TuMV-infected *Nicotiana benthamiana* Domin plants inoculated with the infectious plasmid p35STunos that contains a cDNA of the TuMV genome isolate YC5 from calla lily (*Zantesdeschia* sp) (GeneBank AF530055.2) under the control of the cauliflower mosaic virus 35S promoter and the *nos* terminator (Chen et al. 2003) as described elsewhere (González et al. 2019, Corrêa et al. 2020). After plants showed symptoms of infection, they were pooled and frozen with liquid N_2. This frozen plant tissue was homogenized into a fine powder using a Mixer Mill MM400 (Retsch GmbH, Haan, Germany). For inoculations, 0.1 g of powder was diluted in 1 mL inoculation buffer [50 mM phosphate buffer (pH 7.0), 3% PEG6000, 10% Carborundum] and 5 μL of the inoculum was gently rubbed onto two leaves per plant. As a control, another set of plants were mock-inoculated only with inoculation buffer. Plants were all inoculated when they reached growth stage 3.5 in the Boyes et al. (2001) scale. This synchronization ensures that all hosts were at the same phenological stage when inoculated.

VPg mutations D113G and R118H were introduced by inverse PCR site-directed mutagenesis in the p35STunos plasmid using the Quikchange II XL kit (Agilent Technologies, Santa Clara, CA, USA) and following the indications of the manufacturer, resulting in plasmids p35STunos-VPg^{D113G} and p35STunos-VPg^{R118H}. Plasmids were purified using the ZymoPURE II Plasmid Miniprep kit (Zymo Research, Irving, CA, USA) and resuspended in sterile water.

For evaluation of the mutated VPg alleles, wild-type, *eif(iso)4e* and *rhd1-1* plants were inoculated with p35STunos, p35STunos-VPg^{D113G} and p35STunos-VPg^{R118H}. One leaf per plant was inoculated by gentle abrasion after applying 3 μg of plasmid DNA diluted in 6 μL of water supplemented with 10% Carborundum.

2.5. Infectivity, symptoms progression, and quantification of viral load

The number of infected symptomatic plants, out of 20, as well as the severity of symptoms in a semi-quantitative scale in which zero means no symptoms and 5 systemic necrosis [Fig. 1 in Butković et al. (2021)] were monitored every day until 14 days post-inoculation (dpi). As a control, another set of mock-inoculated plants was treated in the same way. This experiment was repeated in two independent blocks separated by 1 year. Plants were randomized irrespective of their genotypes and inoculated blindly. After each day observations, the positions of the plants in the tray and the position of the trays in the growth chamber were randomly changed.

Viral loads were measured 14 dpi in four different pools of five whole aerial parts of infected plants each, by absolute real-time quantitative RT-PCR (RT-qPCR) using a TuMV standard curve and the primers TuMV F117-fw ($5'$CAATACGTGCGAGAGAAGCACAC$_{3'}$)

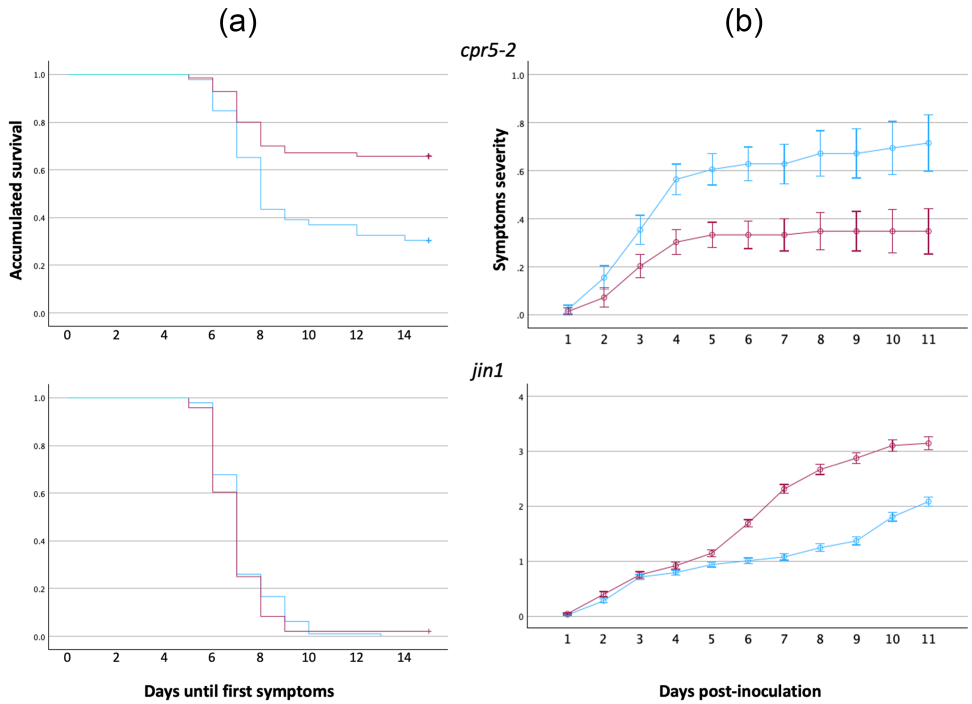

Figure 1. Phenotypic effect of VPg alleles D113G and R118H in disease progression and symptoms severity. (a) Survival curves. (b) Progression of disease severity. The upper row shows the comparison between TuMV-VPg^{wt} and TuMV-VPg^{D113G} in resistant *cpr5-2* plants. The lower row shows the comparison between TuMV-VPg^{wt} and TuMV-VPg^{R118H} in susceptible *jin1* plants. Blue lines and symbols always correspond to TuMV-VPg^{wt}, red lines and symbols to the corresponding mutant being compared.

and F118-rv ($^{5'}$TAACCCCTTAACGCCAAGTAAG$_{3'}$) that amplify a 173-nucleotide fragment from the CP cistron of TuMV genome, as previously described (Corrêa et al. 2020). Briefly, standard curve consisted of nine serial dilutions of the *in vitro* synthesized TuMV genome prepared in total plant RNA purified from healthy *A. thaliana* plants. Amplification reactions were run in a 20-μL volume using the qPCRBIO SyGreen 1-step Go Hi-ROX System (PCRBiosystems, London, UK) and the recommended manufacturer's instructions in an ABI StepOne Plus Real-time PCR System (Applied Biosystems, Foster City, CA, USA). An initial RT phase of 10 min at 45°C and 2 min at 95°C was followed by a PCR stage with the following cycling conditions: 40 cycles of 5 s at 95°C and 25 s at 60°C, and a final melting curve profile analysis that consisted of 15 s at 95°C, 1 min at 60°C, and 15 s at 95°C. As negative controls, total plant RNA (noninfected control) and water were included in the analysis. Quantitative reactions were run as three technical replicates per sample and results were analyzed using the StepOne software 2.2.2 (Applied Biosystems).

2.6. Determination of TuMV consensus sequence

The consensus sequences of the viral genomes accumulated at the end of the infection processes were generated as described elsewhere (e.g. Navarro et al. 2022). In short, total RNAs were obtained and amplified by high-fidelity RT-PCR using the AccuScript Hi-Fi (Agilent Technologies) reverse transcriptase and Phusion DNA polymerase (Thermo Scientific) following the manufacturer's instructions. Each complete TuMV genome was amplified as three overlapping amplicons using three specific sets of primers and the amplification conditions described by Navarro et al. (2022). PCR products were purified with the MSB Spin PCRapace kit (Stratec Molecular, Coronado, CA, USA) and then Sanger-sequenced by Novogene Europe Co. Ltd (Cambridge, UK). Full-length consensus viral sequences were obtained assembling the sequences of the three amplified products by using the Genious R9.0.2 program (Dotmatics, Bishop's Stortford, UK). No additional mutations were found in any of the VPg clones.

2.7. Host gene expression analysis by relative RT-qPCR

For the analysis of *RHD1* and *TGA1* expression, RNA was purified with the Quick-RNA Plant Miniprep kit (Zymo Research) following the protocol recommended by the manufacturer. RT-qPCR was performed in an ABI OneStep Plus Real-time PCR System (Applied Biosystems) from 50 ng RNA using the qPCRBIO SyGreen 1-step Go Hi-ROX System from (PCRBiosystems). The *AT1G13320* corresponding to the *PROTEIN PHOSPHATASE 2A SUBUNIT A3* (*PP2AA3*) gene was used as endogenous reference (Czechowski et al. 2005). The primers used for the amplification were pp2aa3-fw ($^{5'}$TTGGTGCTCAGATGAGGGAGAG$_{3'}$), pp2aa3-rv ($^{5'}$TTCACCAGCTGAAAGTCGCTTAG$_{3'}$), rhd1-fw ($^{5'}$TATCGGAACCACCGCTTACG$_{3'}$), rhd1-rv ($^{5'}$CGGTGGAAGTTACGGTGACA$_{3'}$), tga1-fw ($^{5'}$ACGAACCTGTCCATCAATTCGG$_{3'}$), and tga1-rv ($^{5'}$CCATGGGAAGTATCCTCTGACACG$_{3'}$). For expression in leaves, plants were grown for about 4 weeks [growth stage ~3.70 in the Boyes et al.'s (2001) scale].

2.8. Statistical analyses

Quantitative specificity α-galactosidase assays were conducted per interactor and VPg allele, with repetitions ranging from one to five times (median 2) in independent blocks. To mitigate potential block effects, individual measures were normalized by the mean of the VPg^{wt} allele estimated in the corresponding block. Normalized data underwent analysis using Welch's robust one-way ANOVA, and effect magnitudes were assessed using the η^2 statistic. Conventionally, $\eta^2 < 0.05$ are considered small, $0.05 \leq \eta^2 < 0.15$ as medium, and $\eta^2 \geq 0.15$ as large effects.

Relative expression data for *RHD1* and *TGA1* were fitted to a generalized linear model (GLM) with infection status (mock-inoculated vs TuMV-VPg^{wt} infected) and days post-infection (dpi) as orthogonal factors, utilizing a Gamma distribution and log-link function. In this context, the magnitude of effects was assessed using the η_P^2, with similar criteria than for η^2 above.

The number of infected plants, out of 24 observed for wild-type and *cpr5-2* and *jin1* plants ($n = 3$ blocks; section 3.1), or out of 20 observed for wild-type and *rhd1* plants ($n = 2$ blocks; section 3.5), were independently analyzed using Kaplan-Meier survival analysis. Blocks were treated as experimental replicates. Pairwise comparisons of the median time to the appearance of first symptoms for each VPg allele were performed using log-rank tests. Symptom severity progression data were independently fitted to repeated-measures ANOVAs, with dpi as an intra-individual factor and VPg allele, plant genotype, and experimental block as inter-individual orthogonal factors. The magnitude of effects was evaluated using the η_P^2 statistic.

Viral load data were fitted to a GLM with plant genotype and VPg allele as orthogonal factors, and experimental block nested within the interaction of the two orthogonal factors, employing a Gaussian distribution and identity-link function. The magnitude of effects was assessed using the η_P^2 statistic.

In all reported pairwise *post hoc* tests, the Bonferroni sequential method was applied.

2.9. Homology modeling

Models were generated with MODELLER version 10.4 (Webb and Sali 2016). For the *A. thaliana* eIF(iso)4E, and its paralogs eIF4E and nCBP, the X-ray structures of eIF4E from *Cucumis melo* (Miras et al. 2017), *Pisum sativum* (Ashby et al. 2011), and *Mus musculus* (Rydzik et al. 2017, Wan et al. 2020, Wojcik et al. 2021) were used as templates (Supplementary Fig. S1). The model of the VPg protein from TuMV was inferred using the nuclear magnetic resonance (NMR) structure of the PVY homolog (Coutinho de Oliveira et al. 2019). Input alignments were generated with MUSCLE (Edgar 2004). In each case, the model lowest-energy model out of 100 structures was selected and submitted to a final round of refinement using ROSETTA's relax protocol (Conway et al. 2014).

2.10. Docking

Docking was performed with the Monte-Carlo-based multi-scale docking algorithm implemented in RosettaDock (Chaudhury et al. 2011). In each case, high-energy rotamers were removed prior to docking using the Docking Prepack application from ROSETTA (Wang et al. 2007). For the eIF(iso)4E and VPg docking model, structures were prepositioned near each other with the binding pockets facing each other using HADDOCK (Dominguez et al. 2003, Van Zundert et al. 2016, Honorato et al. 2021). In this case, ambiguous interaction restraints (AIRs) were generated using a combination of NMR chemical shift perturbations (Coutinho de Oliveira et al. 2019), mutagenesis data on the eIF4E/eIF(iso)4E—VPg system (Monzingo et al. 2007, Roudet-Tavert et al. 2007, German-Retana et al. 2008, Ashby et al. 2011, Pérez et al. 2012, Svanella-Dumas et al. 2014), and experimental data from Martínez et al. (2023). Unfolded and mobile regions were removed from both proteins and docking site constraints for residues known to be in contact in the eIF(iso)4E/VPg interaction were included in local docking protocol (Supplementary Fig. S2). A total of 1000 decoys were generated during the docking perturbation runs. Residues in the interface of the selected model were refined using a high-resolution full atom minimization protocol (Conway et al. 2014). After this step, the mobile regions of VPg and eIF(iso)4E were included using MODELLER, and an optimal conformation was recalculated using the kinematic closure method in ROSETTA (Mandell et al. 2009) (Supplementary Fig S2). The final complex was further refined using a molecular dynamic simulation in explicit solvent with NAMD (Phillips et al. 2020). This step was performed using periodic boundary conditions in a water box with a 10 Å padding, 0.15 meter NaCl, and a temperature of 298 K (Spivak et al. 2023). Docking of RHD1 and the VPg protein was performed using a global docking protocol using the AlphaFold RHD1 model available at Uniprot (Jumper et al. 2021). Docking was performed separately on N- and C-terminal Zn-finger and homeobox domains, respectively. After minimization, structures were fitted using a global docking protocol using 10 000 decoys for each RHD1 domain. Other RHD1 PPIs were pulled out from STRING database version 12.0 (Szklarczyk et al. 2023).

3. Results and discussion

3.1. Phenotypic effects of VPg^{D113G} and VPg^{R118H} alleles in their local hosts cpr5-2 and jin1

Prior to any further analysis, we sought to confirm that the two VPg mutations, by themselves, have and affect in disease progression and symptoms severity in the local hosts in which they were selected. In resistant *cpr5-2* plants, the appearance of symptoms was 24% delayed upon inoculation with TuMV-VPg^{D113G} (12.400 ±0.441 dpi) than in plants inoculated with TuMV-VPg^{wt} (10.000 ±0.540 dpi) (Fig. 1a upper panel, log-rank test: $\chi^2 = 13.226$, 1 d.f., $P < .001$). Likewise, symptoms were 47.9% weaker in plants infected with TuMV-VPg^{D113G} than with the wild-type virus (Fig. 1b upper panel, pairwise comparisons: $P < .001$). Despite this difference in average symptomatology, no differences in the rates of symptoms appearance were observed between both viruses (Fig. 1b middle panel, test of differences in slopes: $F_{2.643,111.000} = 1.863$, $P = .143$, $\eta_P^2 = 0.017$).

In susceptible *jin1* plants, no significant difference in the timing of symptoms appearance was observed between TuMV-VPg^{R118H} (7.021 ±0.217 dpi) and TuMV-VPg^{wt} (7.177 ±0.134 dpi) (Fig. 1a lower panel: $\chi^2 = 0.835$, 1 d.f., $P = .361$). In this case, however, the symptoms developed by infected plants were 68.2% stronger for the TuMV-VPg^{R118H} virus (Fig. 1b lower panel: $P < .001$) and became more severe in a faster pace (Fig. 1b lower panel: $F_{4.022,139.000} = 53.855$, $P < .001$, $\eta_P^2 = 0.279$).

In conclusion, the two VPg mutant alleles showed significant effects either in the speed at which symptoms appeared, their severity, or both.

3.2. HT-Y2H screens and evaluation of differences in affinity between VPg variants and host interactors

Three screens were conducted in parallel using VPg^{wt}, VPg^{D113G}, and VPg^{R118H}, as the respective bait proteins. No major differences in protein accumulation were found for all three baits by Western-blot using a monoclonal antibody against the GAL4 DNA-binding domain (Supplementary Fig. S3). The number of clones screened ranged from 2×10^7 to 2.5×10^7 per variant, with a mating efficiency of 30–35%. Initially, the number of clones selected were 159 for VPg^{wt}, 156 for VPg^{D113G}, and 158 for VPg^{R118H}. These clones were further validated through a second round of more rigorous selection, removal of duplicates, and semiquantitative evaluation of binding specificity after plasmid rescue and yeast retransformation, retaining 17 clones for VPg^{wt}, 21 for VPg^{D113G}, and 18 for VPgR^{118H}. Subsequently, a quantitative α-galactosidase activity assay was performed with these clones. Only the 19 clones

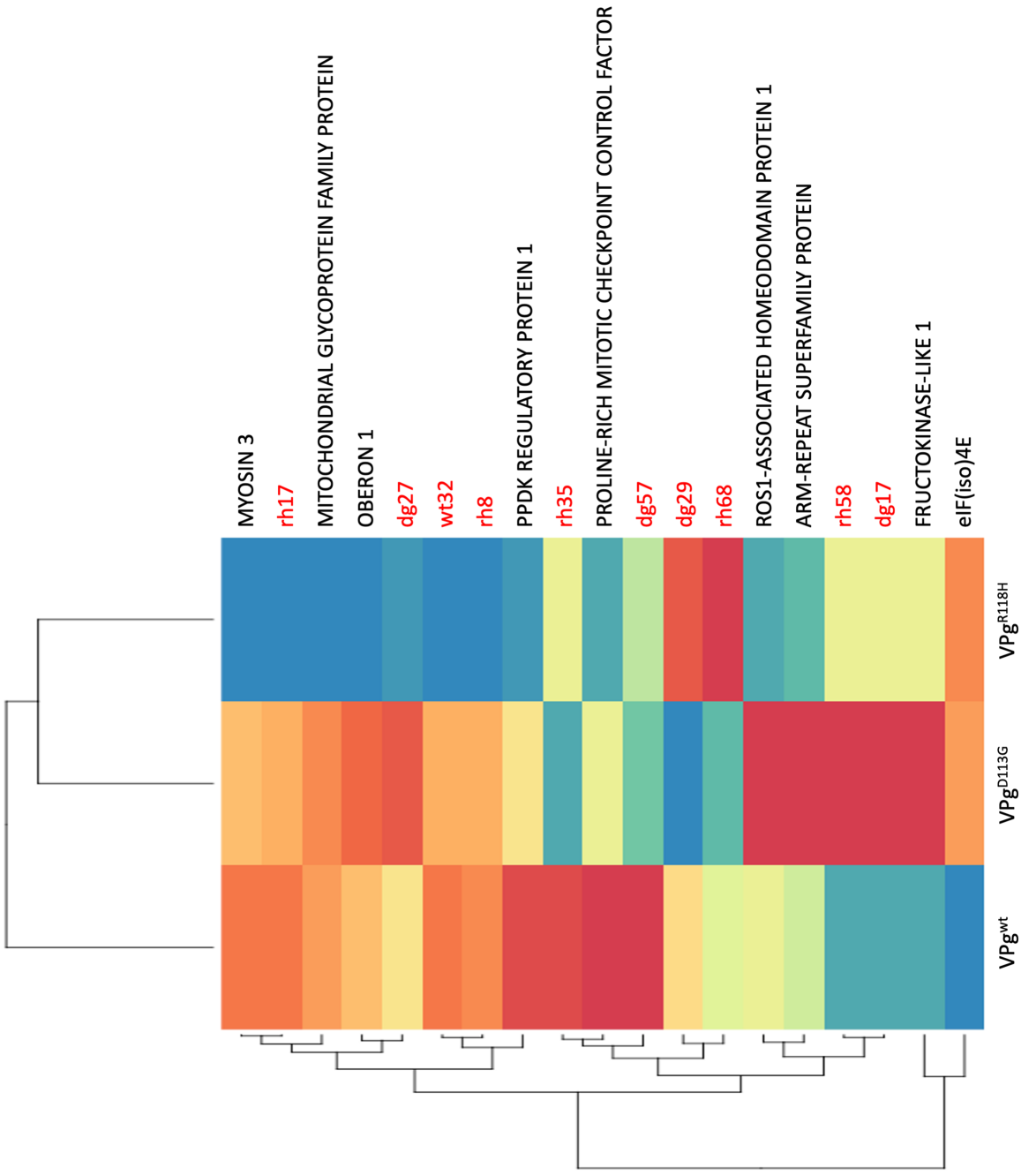

Figure 2. Heatmap constructed from the estimated binding affinities between the three different VPg alleles (wild-type, D113G, and R118H) and the 19 host proteins identified in the HT-Y2H screening. Gene names are only provided for interactors for which statistically significant differences with VPg^{wt} were found and further identified by sequencing. Interactors for which no significant differences in binding affinity were observed are indicated in red. Labels starting with "dg" correspond to those found in the screening against VPg^{D113G}, "rh" to those found in the screening against VPg^{R118H}, and "wt" against the VPg^{wt} allele. Color scale: the more intense blue corresponds to stronger affinities than for VPg^{wt}, whereas stronger red corresponds to weaker (yet quantifiable) affinities than for VPg^{wt}.

displaying significant statistical differences among alleles were subjected to gene identification through sequencing (Fig. 2). Following sequencing, two clones selected for VPg^{D113G} corresponded to *AT5G42780*, while two clones selected for VPg^{wt} matched with *AT5G35620*. Consequently, we identified 19 host proteins that interact differentially among the three VPg alleles.

Figure 2 depicts a heatmap constructed based on the binding affinities similarity matrix among the 19 host proteins and the three VPg alleles. Among the interactors, nine exhibited a significant overall difference among the three VPg alleles (Supplementary Fig. S4). The smallest significant effect was observed with *AT2G19270*, which encodes the *PROLINE RICH MITOTIC CHECKPOINT CONTROL FACTOR* (PRCC). PRCC is involved in regulating protein modifications and signal transductions (Welch's robust ANOVA: $F_{2,25.451} = 4.326$, $P = .024$, $\eta^2 = 0.171$). On the other hand, the most substantial effect was observed with *AT5G35620*, the locus encoding the well-characterized VPg interactor eIF(iso)4E protein ($F_{2,67.604} = 675.852$, $P < .001$, $\eta^2 = 0.958$).

Applying Bonferroni *post hoc* pairwise difference tests, we compared the affinity values between VPg^{wt} and each of the 19 host interactors with those observed for the two VPg mutants, revealing remarkably diverse effects. As illustrated in Fig. 2, these 19 proteins can be categorized into three distinct groups. In the following discussion, we will delve into the host proteins exhibiting differential binding strength with the VPg alleles. The first group comprises two proteins whose interactions are significantly more robust with VPg^{wt} than with either of the two mutant alleles. These proteins are: (i) the aforementioned eIF(iso)4E ($P < .001$; 90.50% weaker interaction) and (ii) the FRUCTOKINASE-LIKE 1 (FLN1) protein, a member of the pfkB-carbohydrate kinase family encoded by locus *AT3G54090* ($P < .001$; 36.54% weaker interaction). FLN1 serves as a potential plastidial target of thioredoxin z and is crucial for proper chloroplast development. Its role extends to the regulation of plastid-encoded polymerase (PEP)-dependent chloroplast transcription. Consequently, *fln1* mutants exhibit aberrant chloroplast development, general developmental defects, and impaired PEP-dependent transcription (Gilkerson et al. 2012).

The second group in Fig. 2 is the most heterogeneous, encompassing three host proteins that exhibit either no differences with VPg^{wt} or variable effects with VPg^{D113G} and VPg^{R118H}. (i) The *AT5G62580* locus encodes ARM-REPEAT SUPERFAMILY PROTEIN and demonstrates a 28.76% reduction in binding strength with VPg^{D113G} compared to VPg^{wt} ($P = .025$), while it shows no significant effect on VPg^{R118H} ($P = 1.000$). This family of proteins binds to microtubules, impacting cellular organization and organ growth (Buschmann et al. 2004). Martínez et al. (2023) already described this protein as an interactor of NIb replicase. (ii) The second protein in this group is RHD1 (encoded by *AT5G42780*). RHD1, a zinc finger and homedomain (ZF-HD) protein, interacts with ROS1-ASSOCIATED METHYL-DNA BINDING PROTEIN 1 (RMB1), ROS1-ASSOCIATED WD40 DOMAIN-CONTAINING PROTEIN (RWD40), and REPRESSOR OF SILENCING 1 (ROS1) in a multiprotein complex involved in the base excision repair pathway through DNA demethylation. This interactor was not described by Martínez et al. (2023). Interestingly, RHD1 interacts with the transcriptional regulator TGA1, known to act as a proviral factor via its interaction with NIb (Martínez et al. 2023). RHD1 exhibits a 22.62% decrease in binding affinity with VPg^{D113G} ($P < .001$) but a 17.35% increase with VPg^{R118H} ($P = .003$) compared to VPg^{wt}. (iii) The third member of this group is the product of the *PRCC* gene, involved in the regulation of protein modifications and signal transductions. While VPg^{D113G} shows no differences in binding compared to VPg^{wt} ($P = 1.000$), VPg^{R118H} exhibits 22.5% stronger binding ($P = .029$).

The third group in Fig. 2 comprises four host proteins that exhibit no differences in affinity between VPg^{wt} and VPg^{D113G} but consistently show increased binding strength with VPg^{R118H}. (i) The product of the gene *PYRUVATE ORTHOPHOSPHATE DIKINASE (PPDK) REGULATORY PROTEIN 1* (*RP1*) (*AT4G21210*) demonstrates 47.15% stronger binding with VPg^{R118H}. RP1, a bifunctional serine/threonine kinase and phosphorylase, is involved in the dark/light-mediated regulation of PPDK by catalyzing its phosphorylation/dephosphorylation (Chastain et al. 2007). Notably, RP1 was not described by Martínez et al. (2023). (ii) The second host protein in this group is OBERON 1 (OBE1), encoded by locus *AT3G07780*; this interaction was previously described by Martínez et al. (2023). OBE1, a nuclear PHD finger protein, interacts with WRKY transcription factors, forming complexes that bind to histones (via the PHD finger) and repress the transcription of many stress-responsive genes (Du et al. 2023). (iii) The MITOCHONDRIAL GLYCOPROTEIN FAMILY PROTEIN encoded by locus *AT1G15870* binds 36.19% more strongly with VPg^{R118H} than with VPg^{wt}. Unfortunately, no information about the function of this glycoprotein in the context of infection is currently available. (iv) The MYOSIN 3 (MYOS3) protein encoded by locus *AT3G58160*, a class XI myosin gene, is involved in the trafficking of Golgi stacks, peroxisomes, and mitochondria in root hairs and leaf epidermal cells (Peremyslov et al. 2008). Class XI myosin genes have been shown to play important and diverse roles in virus replication. For example, Amari et al. (2014) demonstrated that the inactivation of myosin XI genes in *Nicotiana benthamiana* affected the functioning of the endoplasmic reticulum, resulting in the aggregation of the movement protein of tobacco mosaic virus and the altered intracellular distribution of the viral replicase. MYOS3 binds to VPg^{R118H} 27.51% more strongly than to the VPg^{wt} allele ($P = .007$).

In a broad context, changes in host–virus PPI networks can deeply affect the rates of virus and host evolution. The consequences on viral evolution are multiple: (i) the virus faces new challenges in adapting to the host intra-cellular environment. This intense selective pressure can result in acceleration in the rate of molecular evolution, as the virus fixes new mutations to better interact with host proteins (Belshaw et al. 2011, El-Haddad et al. 2023). (ii) As the virus undergoes mutations to adapt to the new PPI landscape, some of these mutations may give rise to new strains with unique characteristics (Almasy et al. 2021). (iii) Virus' pathogenicity can be deeply affected by changes in PPIs. If a virus finds a new, more efficient way to interact with its host proteome, it might cause more severe illness. Conversely, if the changes disrupt critical interactions, the virus could become attenuated. (iv) Adaptations that enhance fitness in the context of a host genotype might decrease it in another, resulting in specialized viral lineages, or in effects that are host genotype-independent, thus rendering generalist viral lineages (Pepin et al. 2006, Elena 2017). (v) Lastly, from the perspective of the host, a change in the PPI network that involves novel host interactors would result in a new strong selective pressure to evolve these new viral targets. However, it has been shown that viruses usually target highly conserved essential host proteins (Enard et al. 2016, Martínez et al. 2023) and, therefore, the balance between two opposed selective pressures will be determined by the essentiality of the novel viral targets.

3.3. TuMV infection affects the expression of RHD1 and TGA1

As outlined in the Introduction, VPg interacts with both the viral replicase NIb and the host factor RHD1. Additionally, both NIb and RHD1 interact with the transcriptional regulator TGA1, identified as a proviral factor by Martínez et al. (2023) for the first time. To assess the impact of TuMV infection on the expression of these crucial genes, a time-course analysis of *RHD1* and *TGA1* expression was conducted via relative RT-qPCR in three pools of mock- and TuMV-VPg^{wt}-inoculated wild-type plants. Figure 3 presents the results of these experiments.

In the case of *RHD1*, overall effects were observed between infected and non-infected plants (GLM: $\chi^2 = 28.568$, 1 d.f., $P < .001$, $\eta^2_P = 0.814$) and across the experimental time ($\chi^2 = 87.164$, 3 d.f., $P < .001$, $\eta^2_P = 0.942$). More notably, a highly significant interaction between these two factors was detected ($\chi^2 = 102.188$, 3 d.f., $P < .001$, $\eta^2_P = 0.953$). This interaction is explained by gene expression in mock-inoculated plants being consistently low and stable over time. In sharp contrast, expression in infected plants was significantly lower (1.5- to 2.4-fold range; $P < .001$) at all time points except at 6 dpi when *RHD1* expression surged 20-fold higher in infected plants ($P < .001$). By negatively affecting RHD1 expression, the virus might interfere with the formation of the ROS1 complex,

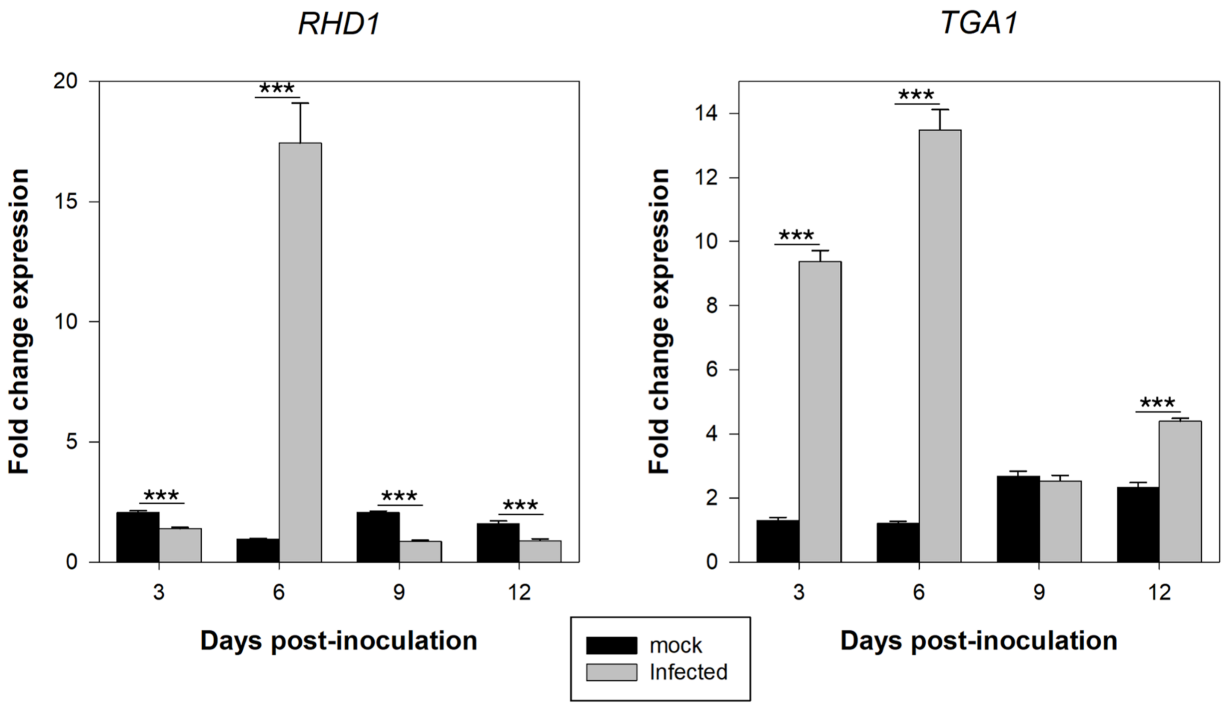

Figure 3. Effect of TuMV-VPg^{wt} infection upon expression of VPg direct (*RHD1*) and indirect (*TGA1*) interactors. Significance levels (sequential Bonferroni *post hoc* tests: *** $P < .001$.

resulting in less demethylation of immunity genes and hence in a weaker antiviral response. The observed pulse-like expression pattern is well suited for coordinating innate immune antiviral responses, fine-tuning cellular processes without committing to prolonged changes in gene activity (e.g. Czerkies et al. 2018).

Concerning the effect of infection on *TGA1* expression, both infection status ($\chi^2 = 100.553$, 1 d.f., $P < .001$, $\eta_p^2 = 0.980$) and dpi ($\chi^2 = 39.247$, 3 d.f., $P < .001$, $\eta_p^2 = 0.953$) had significant effects on *TGA1* expression levels. These effects are not independent ($\chi^2 = 89.968$, 3 d.f., $P < .001$, $\eta_p^2 = 0.975$), as infected plants exhibit enhanced expression over the time course. Maximum differences with non-infected plants were observed at the two earlier time points (7.2- and 11.2-fold higher, respectively; $P < .001$), followed by a reduction to non-significant differences at 9 dpi ($P = .570$) or a 1.9-fold higher expression at the latest sampled time point ($P < .001$). This biphasic step-down expression profile reflects a dynamic regulation of *TGA1* gene activity. The initial high expression phase would be associated with an acute response to the initial infection, while the reduction may represent a shift to a more sustained level of expression compatible with TuMV overcoming defenses and stabilizing a successful infection.

TGA1 regulates plant defense in a manner independent of NPR1 (Shearer et al. 2012). It accomplishes this by inducing the expression of key transcription factors, such as *SYSTEMIC ACQUIRED RESISTANCE DEFICIENT 1* and *CALMODULIN-BINDING PROTEIN 60 g*. These transcription factors, in turn, target various essential regulators of plant defense, including enzymes crucial for the synthesis of SA (Sun et al. 2018). Upon a pathogen attack, SA levels surge, triggering two distinct responses: (i) the activation of *NPR1*, leading to the expression of pathogenesis-related genes critical for reinforcing SAR against subsequent pathogen assaults (Zavaliev and Dong 2023) and (ii) the enhancement of RNA-silencing antiviral defense (Alamillo et al. 2006). In sharp contrast with the observed resistance of *tga1* plants to TuMV infection (Martínez et al. 2023), Shearer et al. (2012) reported increased susceptibility to *Pseudomonas syringae*. This discrepancy among pathogens raises intriguing questions about whether the activation of *TGA1* during infection is a specific plant response or a consequence of a virus-induced overexpression.

3.4. Eif(iso)4e resistance to TuMV infection is not affected by the three VPg alleles

Sets of 20 plants of genotypes *eif(iso)4e* and WT were individually inoculated with the three different VPg alleles. Daily records were kept for both the number of infected plants and the severity of symptoms. A notable initial observation was that none of the 20 *eif(iso)4e* plants exhibited any infection symptoms, irrespective of the VPg allele carried by the inoculated TuMV. The possibility of this negative result being attributed to failed inoculation trials was considered. To eliminate this potential explanation, an additional 68 wild-type plants were inoculated with TuMV-VPg^{wt}. With a sample size of 88 wild-type plants, the probability of infecting a fully susceptible WT plant with TuMV-VPg^{wt} was estimated based on the number of positive events (86) observed after inoculating all the WT plants. Using the LaPlace point estimator and the adjusted Wald 95% confidence interval method, the success rate was calculated to be 0.967 (0.916, 0.999). Therefore, even in the less favorable situation (i.e. the lower limit of the confidence interval), the likelihood of failing 20 independent inoculation events of fully susceptible plants with TuMV-VPg^{wt} would be given by the Bernoulli process $(1–0.916)^{20} = 3.06 \times 10^{-22}$.

The same rationale was applied to the two mutant VPg alleles, where 20 out of 20 inoculated WT plants resulted in symptomatic infections. In this case, the LaPlace estimation of success rate was 0.955 (0.859, 1.000), and the Bernoulli measure for the less

favorable situation was 1.007×10^{-17}. Consequently, we can confidently conclude that *eif(iso)4e* plants are fully resistant to TuMV YC5 infection, regardless of the VPg allele carried by the virus. This observation is in agreement with Bastet et al. (2019), who showed that knock-out of *eIF(iso)4E* resulted in complete plant resistance to, while knock-out of *eIF4E1* had no effect in, TuMV CDN1 accumulation. Interestingly, these authors also showed that TuMV-VPg^{N163Y} and -VPg^{E116G} mutants broke the resistance conferred by the knock-out *eIF(iso)4E*.

Many recessive resistance genes against plant virus such as *Potyvirus*, *Carmovirus*, *Cucumovirus*, or *Potexvirus* encode members of the eIF4E (*eIF4E*, *eIF(iso)4E*, and recently *nCBP*; Keima et al. 2017) and eIF4G, whose loss inhibits viral infection. The involvement of members of the *eIF(iso)4E* and *eIF(iso)4G* gene families has been widely described for potyvirus infection in wild and crop species (Truninger and Aranda 2009). Strikingly, the effect of inactivating *eIF4E1* was highly unpredictable among potyviruses: while its inactivation conferred resistance to clover

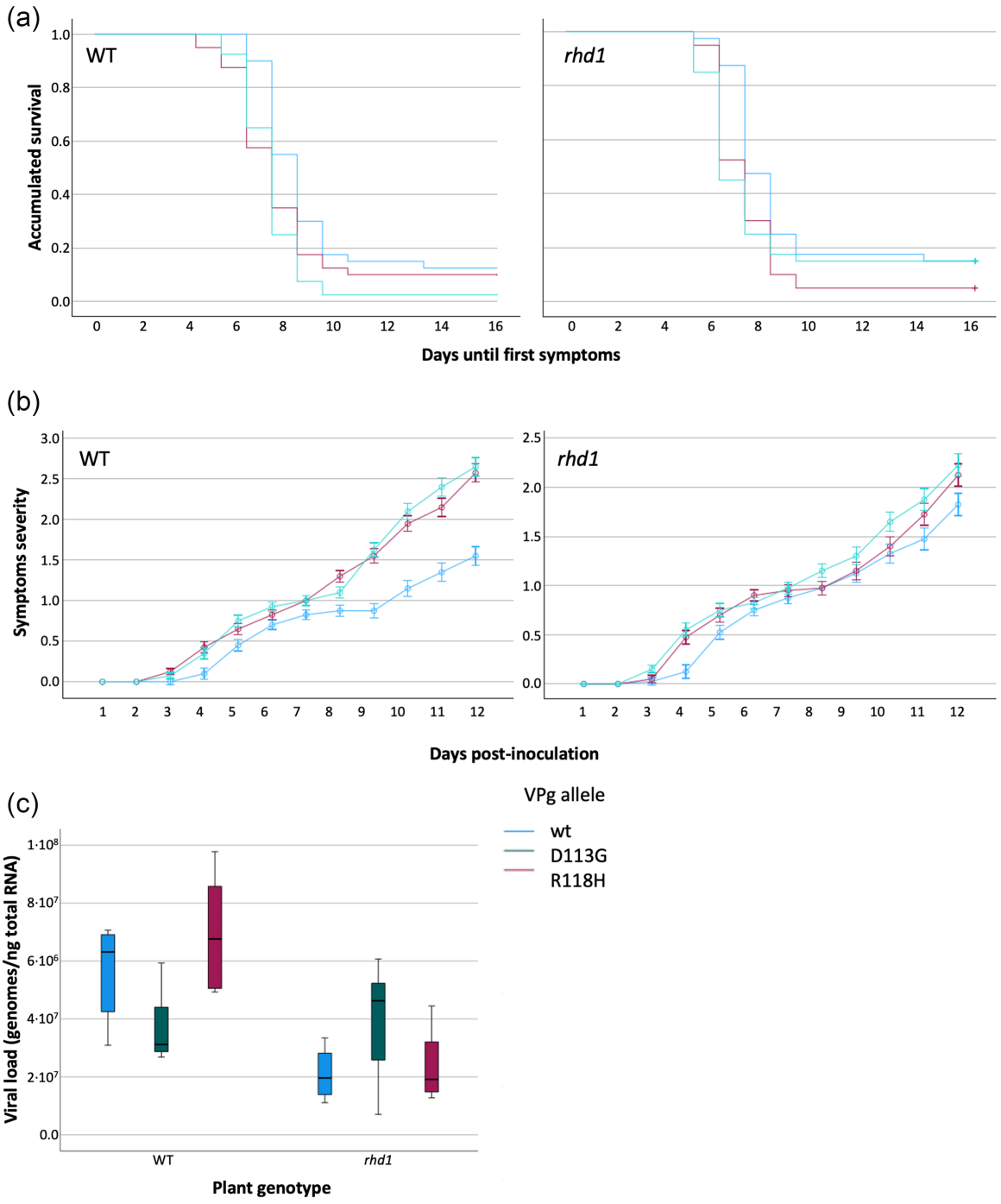

Figure 4. (a) Survival curves representing the number of non-symptomatic plants along time. (b) Progression of disease severity in wild-type and *rhd1* plants infected with TuMV expressing the three different VPg alleles. Error bars represent 95% CI. (c) Differences in viral load measured 14 dpi in four different pools of five infected plants each. Boxes represent interquartile ranks; horizontal lines the median and error bars represent 95% CI. WT: wild-type plants.

yellow vein virus (ClYVV), it also promoted susceptibility to the highly pathogenic TuMV UK1 (Zafirov et al. 2023). Here, we have observed that TuMV YC5 replication strictly depends on the interaction between VPg and a functional eIF(iso)4E. The large differences among UK1 and YC5 strains in pathogenicity and effect on host transcriptomic responses may explain this discrepancy, a possibility to be tested in future experiments.

By contrast, Navarro et al. (2022) were able to experimentally evolve lineages derived from YC5 in *A. thaliana* mutants *i4g1* (deficient for eIF(iso)4 G1), observing different amino acid substitutions in VPg associated with significant fitness increases. These results confirm that eIF(iso)4G is not as essential as eIF(iso)4E for TuMV infection or that its function can be complemented by other translation initiation factors.

3.5. Disease progression in rhd1 mutant plants depends on the VPg allele carried by TuMV

In stark contrast to *eif(iso)4e* plants, *rhd1* plants exhibited variable responses to infection with the three TuMV variants. Firstly, concerning changes in infection rate (Fig. 4a), the mean time to produce visible symptoms was slightly yet significantly affected both by the VPg allele and the plant genotypes (log-rank test: $\chi^2 = 15.168$, 2 d.f., $P < .001$). TuMV-VPg^{wt} produced visible symptoms at 8.750 ±0.475 dpi, regardless the plant genotype. However, TuMV-VPg^{D113G} induced symptoms 5.56% sooner in *rhd1* (7.225 ±0.354 dpi) than in WT (7.650 ±0.483 dpi) plants, with the difference being significant ($\chi^2 = 6.481$, 2 d.f., $P = .039$). In stark contrast, *rhd1* plants infected with TuMV-VPg^{R118H} showed symptoms 9.0% earlier (7.075 ±0.272 dpi) than WT plants (7.775 ±0.564 dpi), with the difference being largely significant ($\chi^2 = 9.450$, 2 d.f., $P = .009$). Therefore, we conclude that VPg^{D113G} and VPg^{R118H} affect the appearance of disease symptoms in plants deficient for RHD1.

Secondly, Fig. 4b illustrates the disease progression curves for the three virus variants in both wild-type and *rhd1* plants. Supplementary Fig. S5 shows images of representative plants of both genotypes infected with each TuMV-VPg variant 12 dpi. In WT plants, large and significant inter-individual differences were observed between the three VPg alleles ($F_{2,228} = 25.720$, $P < .001$, $\eta^2_P = 0.184$), as well as substantial intra-individual differences between dpi ($F_{6.834,779.100} = 11.363$, $P < .001$, $\eta^2_P = 0.898$) and the interaction between intra- and inter-individual factors ($F_{7.867,224.203} = 13.586$, $P < .001$, $\eta^2_P = 0.091$). Overall, TuMV-VPg^{wt} induced milder symptoms (0.704 ±0.033) compared to viruses expressing the two mutant VPg variants (0.958 ±0.033 for VPg^{D113G} and 1.018 ±0.033 for VPg^{R118H}; pairwise comparisons: $P < .001$). The progression of symptoms was similar for the three variants during the first 7 dpi but diverged between VPg^{wt} and the two mutants thereafter. The two mutants were indistinguishable throughout the entire time course of the experiment ($P = .595$). In the case of *rhd1* plants, inter-individual effects were large and significant ($F_{2,234} = 23.338$, $P < .001$, $\eta^2_P = 0.166$), as were intra-individual effects of dpi ($F_{3.121,730.374} = 807.493$, $P < .001$, $\eta^2_P = 0.775$), but not the interaction of the two factors ($F_{6.243,730.374} = 1.497$, $P = .174$, $\eta^2_P = 0.013$). This suggests that differences among virus variants remained constant over time. Overall, indistinguishable symptoms were induced by TuMV-VPg^{wt} and TuMV-VPg^{D113G} (0.752 ±0.048 and 0.871 ±0.048, respectively; $P = .254$), but TuMV-VPg^{R118H} produced consistently more severe symptoms than TuMV-VPg^{wt} (0.954 ±0.048; $P = .011$).

Thirdly, we assessed the efficiency of TuMV carrying different VPg alleles in terms of viral accumulation at 12 dpi. Figure 4c illustrates the comparison between the two plant genotypes and the three VPg alleles. The two orthogonal main factors had a significant effect on viral load, although the magnitude of the effect was small among VPg alleles (plant genotype: $\chi^2 = 226.733$, 1 d.f., $P < .001$, $\eta^2_P = 0.459$; VPg allele: $\chi^2 = 75.113$, 2 d.f., $P < .001$, $\eta^2_P = 0.065$). Nonetheless, the interaction between both factors was highly significant and of large magnitude ($\chi^2 = 196.689$, 2 d.f., $P < .001$, $\eta^2_P = 0.353$), suggesting that the effect on viral load of the VPg alleles was strongly dependent on the expression of *RHD1*. As illustrated in Fig. 4c, viral load was reduced, on average, by 47.93% in *rhd1* plants ($P \leq .018$ in the three pairwise comparisons). Focusing on WT plants, TuMV-VPg^{R118H} showed the highest viral load (6.902 ±0.159)× 10^7 (±1 SE), followed by TuMV-VPg^{wt} (5.675 ±0.132)× 10^7 and TuMV-VPg^{D113G} (3.656 ±0.098)× 10^7. However, in *rhd1* plants, the situation reversed, and the highest viral load was observed for TuMV-VPg^{D113G} (3.954 ±0.327)× 10^7, followed by TuMV-VPg^{R118H} (2.371 ±0.099)× 10^7 and TuMV-VPg^{wt} (2.133 ±0.067)× 10^7. (In all cases, $P \leq .031$ in the three pairwise WT vs *rhd1* comparisons).

At first glance, the observation of earlier and more severe symptoms in *rhd1* plants suggests that the RHD1 protein plays an antiviral role in *A. thaliana*. However, higher TuMV accumulation was noted in WT plants. To reconcile these two observations, one could argue that symptoms may not necessarily correlate with viral accumulation if *RHD1* enhances the plant's tolerance to viral infection (Pagán and García-Arenal 2020). In such a scenario, WT plants expressing *RHD1* might exhibit higher viral accumulation while maintaining mild symptoms. Conversely, if *RHD1* expression is knocked out, even low viral accumulation could rapidly result in more severe symptoms. Interestingly, the level of tolerance appears to be influenced by VPg alleles: viruses carrying the VPg^{wt} and VPg^{R118H} show larger reductions in virus accumulation, whereas viruses carrying the generalist VPg^{D113G} are less affected (Fig. 4c). Notably, unlike the other two alleles, this mutation in the VPg protein reduces its apparent affinity for RHD1 and, therefore, is likely to compromise the interaction. Additional experiments are required to shed light into the link between virus accumulation and symptoms progression mediated by RHD1.

A disassociation between virus accumulation and symptoms severity has relevant implications for the virulence—transmission trade-off. Two classic theories have been brought forward to explain the existence of this trade-off. At the one side, the optimal virulence hypothesis poses that there is an optimal level of virulence that maximizes transmission (Anderson and May 1982, Ewald 1983, Acevedo et al. 2019). Too much virulence can hurt the host too quickly, reducing transmission opportunities, while too little might not produce enough viral load for an effective transmission. Under this hypothesis, selection operates both at the within-host and between-host population levels. At the other side, the short-sighted evolution hypothesis builds upon the idea that within-host evolution might favor higher replication rates and that faster replicating viruses are more virulent because they affect cell homeostasis in a larger extent (Antia et al. 1994, Van Baalen and Sabelis 1995, Lythgoe et al. 2013). This damage is detrimental from between-host transmission if the host deteriorates too quickly. Under this hypothesis, selection operates primarily at the within-host level favoring traits that increase the fitness for the virus within a single host, even if those changes are detrimental to the virus' transmission and overall fitness at the population level. Tests of these two hypotheses in plant virus are still scarce. In agreement with our observation of viral genotype-dependent association between within-host multiplication and virulence, Pagán et al. (2007) found that a positive correlation between cucumber mosaic virus multiplication and virulence may

occur only in some *A. thaliana* genotypes and/or environmental conditions. Likewise, Agudelo-Romero et al. (2008b) found that the positive association between within-host accumulation and virulence depended on the past evolutionary history of TEV on each particular host, with the association being stronger in alternative hosts. However, Doumayrou et al. (2013) demonstrated a virulence—transmission trade-off in the pathosystem cauliflower mosaic virus—*Brassica rapa*. Together, these results challenge the overall validity of the trade-off hypothesis for virulence evolution and emphasize the importance of considering both host and virus genotypes in analyses of host–parasite interactions.

Together with RMB1 and ROS1-ASSOCIATED WD40 DOMAIN-CONTAINING PROTEIN (RWD40), RHD1 is part of the RWD40 complex, which regulates active DNA demethylation by specifically directing ROS1 DNA demethylase to specific target sequences in the *A. thaliana* genome (Liu et al. 2021). The absence of expression of any of the components of the RWD40 complex results in ROS1 mislocalization, hypermethylation of targeted genomic DNA regions, and hypersusceptibility to the hemibiotrophic bacterial pathogen *Pseudomonas syringae*, suggesting a role of the RWD40 DNA demethylation complex in pathogen defense (Liu et al. 2021). One of these regions is localized in the *ROS1* promoter, leading to slightly increased *ROS1* expression. Therefore, in *rhd1* plants, *ROS1* expression is upregulated but its methylated target sequences are not recognized and become hypermethylated compared to WT plants. In addition, TuMV infection also downregulates the expression of *ROS1* (Corrêa et al. 2020), in agreement with the results shown for WT plants in Fig. 3 for most dpi. The sharp *RHD1* induction observed during TuMV infection might be involved in temporally downregulating *ROS1* expression and the subsequent temporal increase in the methylation rate of specific genome sequences, thereby altering gene expression. Moreover, the pulse-like expression of *RHD1* and the drop in expression in *TGA1* observed after 6 dpi (Fig. 3) coincide with the slow-down in symptoms progression observed for TuMV-VPg^{wt}, which stay subsequently milder (roughly speaking in the range 1–2). The two VPg mutants escape from this control, resulting in worsened symptoms.

Altering the epigenetic regulation of host genes is a common feature among plant (Diezma-Navas et al. 2019, Corrêa et al. 2020, 2024) and animal viruses (Rehman et al. 2023). Virus-induced changes in the epigenetic regulation of immunity-related genes add a complex layer to host–virus coevolution. These changes

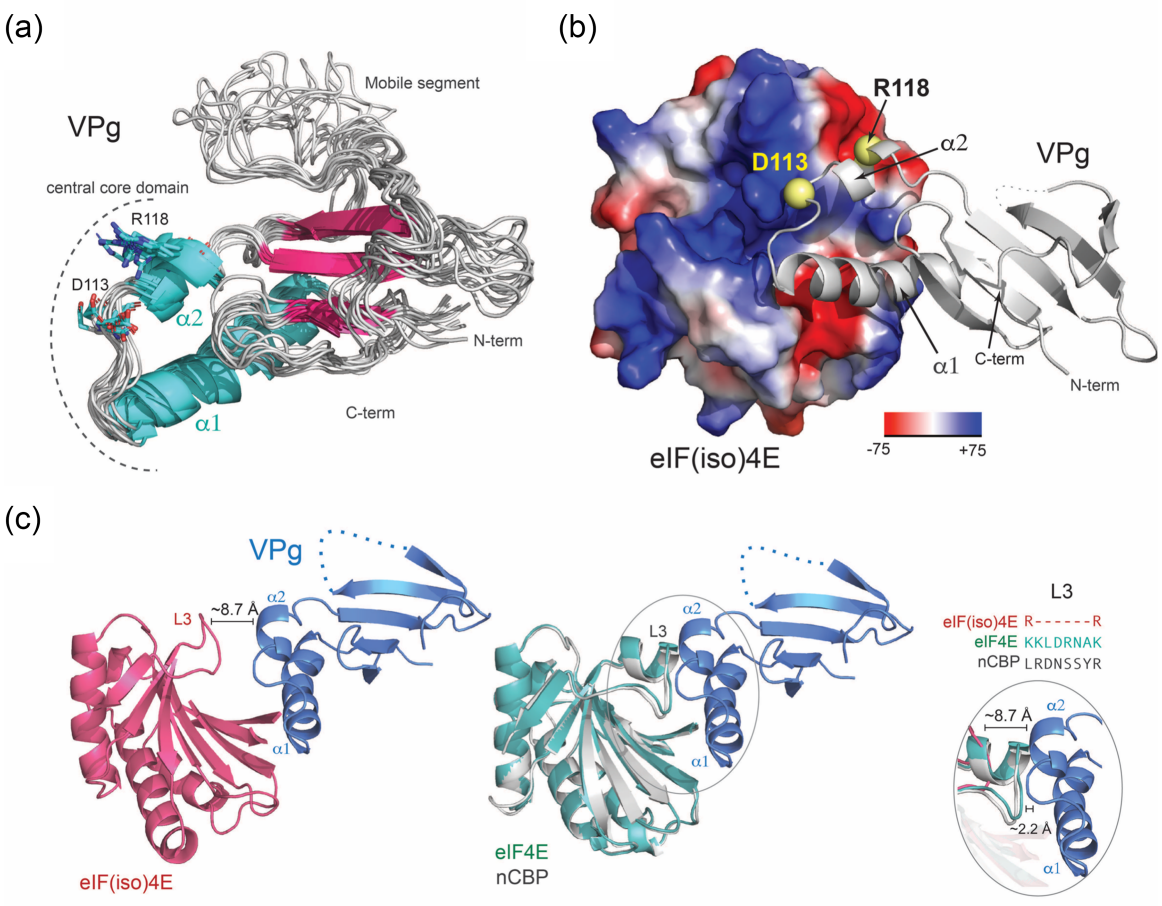

Figure 5. Structural analysis of the *A. thaliana* eIF(iso)4E–TuMV VPg complex. (a) The model of TuMV VPg reveals that D113 and R118 project outwards in a segment comprising the α1-α2 loop and helix α2. The structural ensemble illustrates the dynamical properties of the VPg proteins as determined by molecular dynamics simulations. (b) Analysis of the eIF(iso)4E–VPg docking model suggests that residues D113 and R118 bind to pockets of complementary charges in eIF(iso)4E. The reduced affinity of the D113G and R118H variants probably results from the removal of these ionic interactions. (c) The eIF(iso)4E–VPg (left) docking model explains the resistance in *eif(iso)4e* plants as the paralogous protein eIF4E and nCBP have a bulkier VPg binding region (L3) that is likely to impede binding to TuMV VPg (center). The sequence of the L3 region of the eIF4E homologs in *A. thaliana* and their relative distance to VPg is illustrated in the right panel.

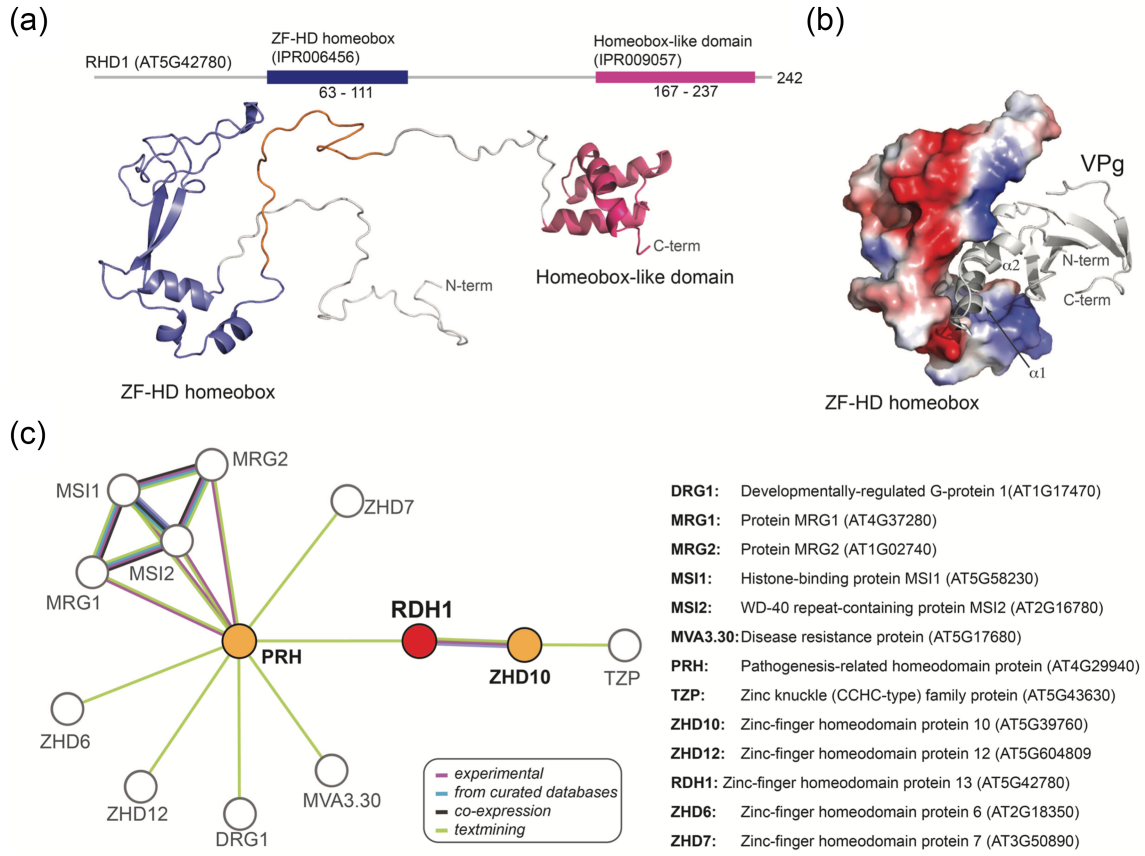

Figure 6. Structural properties of the RHD1 protein from A. thaliana. (a) The AlphaFold modeling and sequences analysis reveal that this protein contains Zn-finger (ZF-HD) and a C-terminal homeobox domain, and unstructured N-terminal and central regions. (b) Global docking of VPg against the homeobox and Zn-finger domains of RHD1 using ROSETTA revealed a potential binding site comprising the central domain of VPg and a crevice in the Zinc-finger region. (c) PPI network of the RHD1 with other A. thaliana proteins according to STRING database.

can modulate the host immune response, affect long-term host adaptation, and drive coevolutionary arms races, highlighting the intricate and dynamic nature of host–virus interactions. Indeed, evolution experiments in mutants for RNA-directed DNA methylation genes and histone modification genes (Mongelli et al. 2022, Navarro et al. 2022, Ambrós et al. 2024) suggest a direct role of these genes in the evolution of virus virulence and within-host accumulation.

3.6. Integrating interaction results with structural analyses

To better understand these differences in interactions, we modeled the interactions of VPg with eIF(iso)4E (Fig. 5) and RHD1 (Fig. 6). First, we modeled the TuMV-VPg/eIF(iso)4E complex using a docking procedure guided by experimental data (Supplementary Fig. S2). Several lines of evidence suggest that the proposed model is close to the real structure: (i) the contact surface involves the central domain of VPg and the cap-binding region of eIF(iso)4E, in agreement with experimental data; (ii) conserved residue R103 in the central domain of VPg binds to eIF(iso)4E in a position equivalent to the guanine base in the m^7G cap, (iii) acidic residues in the segment comprising the α1-α2 loop bind to a region close to the phosphate binding region in eIF(iso)4E, and (iv) experimental data on residues involved int eIF4E–VPg interactions are mostly clustered in the docking interaction surface (Grzela et al. 2006, Roudet-Tavert et al. 2007; Ashby et al. 2011 Svanella-Dumas et al. 2014, Coutinho de Oliveira et al. 2019). Our model also provides a plausible explanation of the effect of the R118H and D113G substitutions on the eIF(iso)4E–VPg interaction (Fig. 5). R118 and D113 are located in a small helical segment predicted to bind to a region with complementary charges in the m^7G cap-binding pocket of eIF(iso)4E (Fig. 5). Based on our model, both VPg mutants are expected to have a weaker binding to eIF(iso)4E. The D113G mutation would remove a negative charge that interacts with a positive surface in eIF(iso)4E. Something similar is expected for the R118H mutation, as histidine is neutral at pH > 6.0; this substitution will remove a positive charge interacting with a negative region of eIF(iso)4E. Therefore, we postulate that the R118H and D113G mutations remove favorable ionic interactions, resulting in the observed reduction in the stability of the eIF(iso)4E–VPg complex.

Our model also explains the resistance of *eif(iso)4e* plants against the three TuMV mutants. Potyviruses selectively require different eIF4E paralogs to establish infection (Duprat et al. 2002, Sato et al. 2005, Nicaise et al. 2007, Gómez et al. 2019). In *A. thaliana*, lettuce mosaic virus (LMV), TEV, and TuMV use eIF(iso)4E, while other potyviruses, such as ClYVV and PVY, use eIF4E (Sato et al. 2005, Zafirov et al. 2023). Structurally, one of the most salient differences between eIF(iso)4E and its paralogs eIF4E and nCBP is the presence of a bulkier segment in the VPg binding region. We propose that due to this steric effect, neither eIF4E nor nCBP can substitute for eIF(iso)4E in the *eif(iso)4e* plants (Fig. 5).

We also used docking to identify a potential VPg binding pocket in the RHD1 protein from *A. thaliana* (Fig. 6). A prediction of structural domains revealed that this protein contains an N-proximal Zn finger domain, a C-terminal homeobox domain, and two unstructured segments comprising the N-terminal and central regions (Fig. 6a). Assuming that binding occurs in the Zn-finger domain and/or in the homeodomain, we performed a global docking of VPg using a refined AlphaFold model of RHD1 (Fig. 6b). The lowest energy complex fitted the VPg core domain within a crevice separating the helical and beta-stranded regions of the Zn-finger domain. This region comprises domains of positive and negative charge that might be affected by the ionization state of the VPg protein.

Figure 6c shows the RHD1 PPIs network generated with STRING. Interestingly, RHD1 interactors mostly belong to the ZF-HD-containing family protein of transcription factors. The direct interactor PATHOGENESIS RELATED HOMEODOMAIN PROTEIN A (PRHA) is a hub that bridges ZF-HDs involved in the regulation of different aspects of plant development and of circadian clock, with MVA3.30, a disease resistance protein of the TIR-NBS-LRR class family, and with MORPH RELATED GENE 1 (MRG1) and 2 (MRG2), both readers of H3K4m3/H3K36m3 methylation marks. Taken together, these interactions further support the possibility that VPg affects epigenetic regulations by interacting with RHD1 and indirectly affects its interaction with other transcription factors and components of the histone methylation machinery. The role of such epigenetic pathways in TuMV infection has been already established (Corrêa et al. 2020, Navarro et al. 2022) and might contribute to the enhanced tolerance to infection of plants accumulating RHD1.

4. Concluding remarks

The results shown above shed light on the complex interplay between TuMV VPg variants, host proteins, and plant defense response, providing valuable insights into the molecular mechanisms underlying virus–host interactions and disease progression in *A. thaliana*. The three different VPg alleles used in our study show differential interactions with plant proteins. Infected plants show altered expression of key genes *eIF(iso)4E*, *RHD1*, and *TGA1*. Mutant plants *eif(iso)4e* show complete resistance to TuMV infection regardless of the VPg allele, confirming its well described essential role in virus replication. Finally, different VPg alleles affect disease progression in *rhd1* mutant plants. VPg^{D113G} and VPg^{R118H} accelerate symptom appearance, while VPg^{wt} induces milder symptoms. This observation suggests that RHD1 modulates the tolerance to viral infection, likely via epigenetic modifications.

This study was mostly focused to explore changes in the VPg interaction resulting from adaptation of TuMV to different *A. thaliana* genotypes. Our results also provide some insights into broader evolutionary questions such as the evolution of virulence-transmission trade-offs or the potential role of epigenetic regulation of immunity genes in the coevolution between viruses and hosts.

Acknowledgements

We thank Francisca de la Iglesia and Paula Agudo for excellent technical assistance and the rest of the EvolSysVir lab members for fruitful discussions.

Supplementary data

Supplementary data is available at *Virus Evolution* online.

Conflict of interest: None declared.

Funding

This work was supported by grants PID2022-136912NB-I00 funded by MCIU/AEI/10.13039/501100011033 and by "ERDF a way of making Europe," and CIPROM/2022/59 funded by Generalitat Valenciana to S.F.E.

Data availability

All raw data are available at https://git.csic.es/SFElena/tumv-evolution-in-a.-thaliana-genotypes-with-deficient-immune-responses.

References

Acevedo MA, Dillemuth FP, Flick AJ *et al.* Virulence-driven trade-offs in disease transmission: a meta-analysis. *Evolution* 2019;**73**:636–47.

Agudelo-Romero P, Carbonell P, Perez-Amador MA *et al.* Virus adaptation by manipulation of host's gene expression. *PLoS One* 2008a;**3**:e2397.

Agudelo-Romero P, de la Iglesia F, Elena SF. The pleiotropic cost of host-specialization in tobacco etch potyvirus. *Infect Genet Evol* 2008b;**8**:806–14.

Aguirre J, Guantes R. Virus-host protein co-expression networks reveal temporal organization and strategies of viral infection. *iScience* 2023;**26**:108475.

Ahmed H, Howton TC, Sun Y *et al.* Network biology discovers pathogen contact points in host protein-protein interactomes. *Nat Commun* 2018;**9**:2312.

Alamillo JM, Saénz P, García JA. Salicylic acid-mediated and RNA-silencing defense mechanisms cooperate in the restriction of systemic spread of plum pox virus in tobacco. *Plant J* 2006;**48**:217–27.

Almasy KM, Davies JP, Plate L. Comparative host interactomes of the SARS-CoV-2 nonstructural protein 3 and human coronavirus homologs. *Mol Cell Proteomics* 2021;**20**:100120.

Amari K, Di Donato M, Dolja VV *et al.* Myosins VIII and XI play distinct roles in reproduction and transport of *Tobacco mosaic virus*. *PLoS Pathog* 2014;**10**:e1004448.

Ambrós S, Olmo-Uceda MJ, Corrêa RL *et al.* Phenotypic and genomic changes during Turnip mosaic virus adaptation to *Arabidopsis thaliana* mutants lacking epigenetic regulatory factors. *Evolution* 2024;**28**:69–85.

Anderson R, May R. Coevolution of hosts and parasites. *Parasitology* 1982;**85**:411–26.

Antia R, Levin BR, May RM *et al.* Within-host population dynamics and the evolution and maintenance of microparasite virulence. *Am. Nat.* 1994;**144**:457–72.

Ashby JA, Stevenson CEM, Jarvis GE *et al.* Structure-based mutational analysis of eIF4E in relation to *sbm1* resistance to pea seed-borne mosaic virus in pea. *PLoS One* 2011;**6**:e15873.

Ayme V, Souche S, Caranta C *et al.* Different mutations in the genome-linked protein VPg of potato virus Y confer virulence on the pvr2 3 resistance in pepper. *Mol Plant-Microbe Interact* 2006;**19**:557–63.

Bastet A, Zafirov D, Giovinazzo N *et al.* Mimicking natural polymorphism in *eIF 4E by CRISPR -Cas9 base editing is associated with resistance to potyviruses*. *Plant Biotechnol J* 2019;**17**:1736–50.

Belshaw R, Pybus OG, Rambaut A. The evolution of genome compression and genomic novelty in RNA viruses. *Genome Res* 2007;**17**:1496–504.

Belshaw R, Sanjuán R, Pybus OG. Viral mutation and substitution: units and levels. *Curr Opin Virol* 2011;**1**:430–35.

Bosque G, Folch-Fortuny A, Picó J *et al*. Topology analysis and visualization of *Potyvirus* protein-protein interaction network. *BMC Syst Biol* 2014;**8**:129.

Boyes DC, Zayed AM, Ascenzi R *et al*. Growth stage-based phenotypic analysis of Arabidopsis: a model for high throughput functional genomics in plants. *Plant Cell* 2001;**13**:1499–510.

Buschmann H, Fabri CO, Hauptmann M *et al*. Helical growth of the *Arabidopsis* mutant *tortifolia1* reveals a plant-specific microtubule-associated protein. *Curr Biol* 2004;**14**:1515–21.

Butković A, González R, Rivarez MPS *et al*. A genome-wide association study identifies *Arabidopsis thaliana* genes that contribute to differences in the outcome of infection with two Turnip mosaic potyvirus strains that differ in their evolutionary history and degree of host specialization. *Virus Evol* 2021;**7**:veab063.

Cervera H, Ambrós S, Bernet GP *et al*. Viral fitness correlates with the magnitude and direction of the perturbation induced in the host's transcriptome: the tobacco etch potyvirus-tobacco case study. *Mol Biol Evol* 2018;**35**:1599–615.

Chastain CJ, Xu W, Parsley K *et al*. The pyruvate, orthophosphate dikinase regulatory proteins of Arabidopsis possess a novel, unprecedented Ser/Thr protein kinase primary structure. *Plant J* 2007;**53**:854–63.

Chaudhury S, Berrondo M, Weitzner BD *et al*. Benchmarking and analysis of protein docking performance in Rosetta v3.2. *PLoS One* 2011;**6**:e22477.

Chen CC, Chao CH, Chen CC *et al*. Identification of turnip mosaic virus isolates causing yellow stripe and spot on calla lily. *Plant Dis* 2003;**87**:901–05.

Conway P, Tyka MD, DiMaio F *et al*. Relaxation of backbone bond geometry improves protein energy landscape modeling. *Protein Sci* 2014;**23**:47–55.

Corrêa RL, Kutnjak D, Ambrós S *et al*. Identification of epigenetically regulated genes involved in plant-virus interaction and their role in virus-triggered induced resistance. *BMC Plant Biol* 2024;**24**:172.

Corrêa RL, Sanz-Carbonell A, Kogej Z *et al*. Viral fitness determines the magnitude of transcriptomic and epigenomic reprogramming of defense responses in plants. *Mol Biol Evol* 2020;**37**:1866–81.

Coutinho de Oliveira L, Volpon L, Rahardjo AK *et al*. Structural studies of the eIF4E-VPg complex reveal a direct competition for capped RNA: implications for translation. *Proc National Acad Sci USA* 2019;**116**:24056–65.

Czechowski T, Stitt M, Altmann T *et al*. Genome-wide identification and testing of superior reference genes for transcript normalization in Arabidopsis. *Plant Physiol* 2005;**139**:5–17.

Czerkies M, Korwek Z, Prus W *et al*. Cell fate in antiviral response arises in the crosstalk of IRF, NF-κB and JAK/STAT pathways. *Nat Commun* 2018;**9**:493.

De Chassey B, Navratil V, Tafforeau L *et al*. Hepatitis C virus infection protein network. *Mol Syst Biol* 2008;**4**:230.

Diezma-Navas L, Pérez-González A, Artaza H *et al*. Crosstalk between epigenetic silencing and infection by tobacco rattle virus in Arabidopsis. *Mol Plant Pathol* 2019;**20**:1439–52.

Dominguez C, Boelens R, Bonvin AM. HADDOCK: a protein-protein docking approach based on biochemical or biophysical information. *J Am Chem Soc* 2003;**125**:1731–37.

Doumayrou J, Avellan A, Froissart R *et al*. An experimental test of the transmission-virulence trade-off hypothesis in a plant virus. *Evolution* 2013;**67**:477–86.

Du P, Wang Q, Yuan D-Y *et al*. WRKY transcription factors and OBERON histone-binding proteins form complexes to balance plant growth and stress tolerance. *EMBO J* 2023;**42**:e113639.

Duprat A, Caranta C, Revers F *et al*. The Arabidopsis eukaryotic initiation factor (iso)4E is dispensable for plant growth but required for susceptibility to potyviruses. *Plant J* 2002;**32**:927–34.

Dyer MD, Murali TM, Sobral BW. The landscape of human proteins interacting with viruses and other pathogens. *PLoS Pathog* 2008;**4**:e32.

Edgar RC. MUSCLE: multiple sequence alignment with high accuracy and high throughput. *Nucleic Acids Res* 2004;**32**:1792–97.

Elena SF. Local adaptation of plant viruses: lessons from experimental evolution. *Mol Ecol* 2017;**26**:1711–19.

El-Haddad K, Adhikari TM, Tu ZJ *et al*. Intra-host mutation rate of acute SARS-CoV-2 infection during the initial pandemic wave. *Virus Genes* 2023;**59**:653–61.

Enard D, Cai L, Gwennap C *et al*. Viruses are a dominant driver of protein adaptation in mammals. *eLife* 2016;**5**:e12469.

Eskelin K, Hafrén A, Rantalainen KI *et al*. Potyviral VPg enhances viral RNA translation and inhibits reporter mRNA translation *in planta*. *J Virol* 2011;**85**:9210–21.

Ewald PW. Host-parasite relations, vectors, and the evolution of disease severity. *Annu Rev Ecol Syst* 1983;**14**:465–85.

Gallois J-L, Charron C, Sanchez F *et al*. Single amino acid changes in the turnip mosaic virus viral genome-linked protein (VPg) confer virulence towards *Arabidopsis thaliana* mutants knocked out for eukaryotic initiation factors eIF(iso)4E and eIF(iso)4G. *J Gen Virol* 2010;**91**:288–93.

German-Retana S, Walter J, Doublet B *et al*. Mutational analysis of plant cap-binding protein eIF4E reveals key amino acids involved in biochemical functions and potyvirus infection. *J Virol* 2008;**82**:7601–12.

Gilkerson J, Perez-Ruiz JM, Chory J *et al*. The plastid-localized pfkB-type carbohydrate kinases FRUCTOKINASE-LIKE 1 and 2 are essential for growth and development of *Arabidopsis thaliana*. *BMC Plant Biol* 2012;**12**:102.

Gómez MA, Lin ZD, Moll T *et al*. Simultaneous CRISPR /Cas9-mediated editing of cassava eIF 4E isoforms nCBP –1 and nCBP –2 reduces cassava brown streak disease symptom severity and incidence. *Plant Biotechnol J* 2019;**17**:421–34.

González R, Butković A, Elena SF. Role of host genetic diversity for susceptibility-to-infection in the evolution of virulence of a plant virus. *Virus Evol* 2019;**5**:vez024.

González R, Butković A, Escaray FJ *et al*. Plant virus evolution under strong drought conditions results in a transition from parasitism to mutualism. *Proc National Acad Sci USA* 2021;**118**:e2020990118.

Grzela R, Strokovska L, Andrieu J-P *et al*. Potyvirus terminal protein VPg, effector of host eukaryotic initiation factor eIF4E. *Biochimie* 2006;**88**:887–96.

Hafrén A, Löhmus A, Mäkinen K. Formation of potato virus A-induced RNA granules and viral translation are interrelated processes required for optimal virus accumulation. *PLoS Pathog* 2015;**11**:e1005314.

Hillung J, Cuevas JM, Valverde S *et al*. Experimental evolution of an emerging plant virus in host genotypes that differ in their susceptibility to infection. *Evolution* 2014;**68**:2467–80.

Honorato RV, Koukos PI, Jiménez-García B *et al*. Structural biology in the clouds: the WeNMR-EOSC ecosystem. *Front Mol Biosci* 2021;**8**:729513.

Jumper J, Evans R, Pritzel A *et al*. Highly accurate protein structure prediction with AlphaFold. *Nature* 2021;**596**:583–89.

Keima T, Hagiwara-Komoda Y, Hashimoto M *et al*. Deficiency of the eIF4E isoform nCBP limits the cell-to-cell movement of a plant

virus encoding triple-gene-block proteins in *Arabidopsis thaliana*. *Sci Rep* 2017;**7**:39678.

Liu P *et al*. A novel protein complex that regulates active DNA demethylation in Arabidopsis. *J Integr Plant Biol* 2021;**63**:772–86.

Lythgoe KA, Pellis L, Frase C. Is HIV short-sighted? Insights from a multistrain nested model. *Evolution* 2013;**67**:2769–82.

Mahmoudabadi G, Phillips R. A comprehensive and quantitative exploration of thousands of viral genomes. *eLife* 2018;**7**: e31955.

Mandell DJ, Coutsias EA, Kortemme T *et al*. Sub-angstrom accuracy in protein loop reconstruction by robotics-inspired conformational sampling. *Na Methods* 2009;**6**:551–52.

Martínez F, Carrasco JL, Toft C *et al*. A binary interaction map between turnip mosaic virus and *Arabidoposis thaliana* proteomes. *Commun Biol* 2023;**6**:28.

Martínez F, Rodrigo G, Aragonés V *et al*. Interaction network of tobacco etch potyvirus NIa protein with the host proteome during infection. *BMC Genomics* 2016;**17**:87.

Melero I, González R, Elena SF. Host developmental stages shape the evolution of plant RNA virus. *Philos Trans R Soc B* 2023;**378**:20220005.

Menche J, Sharma A, Kitsak M *et al*. Uncovering disease-disease relationships through the incomplete interactome. *Science* 2015;**347**:841.

Miras M, Truniger V, Silva C *et al*. Structure of eIF4E in complex with an eIF4G peptide supports a universal bipartite binding mode for protein translation. *Plant Physiol* 2017;**174**:1476–91.

Mongelli V, Lequime S, Kousathanas A *et al*. Innate immune pathways act synergistically to constrain RNA virus evolution in *Drosophila melanogaster*. *Nat Ecol Evol* 2022;**6**:565–78.

Monzingo AF, Dhaliwal S, Dutt-Chaudhuri A *et al*. The structure of eukaryotic translation initiation factor-4E from wheat reveals a novel disulfide bond. *Plant Physiol* 2007;**143**:1504–18.

Moury B, Morel C, Johansen E *et al*. Mutations in potato virus Y genome-linked protein determine virulence toward recessive resistances in capsicum annuum and lycopersicon hirsutum. *Mol Plant-Microbe Interact* 2004;**17**:322–29.

Mukhtar MS, Carvunis A-R, Dreze M *et al*. Independently evolved virulence effectors converge onto hubs in a plant immune system network. *Science* 2011;**333**:596–601.

Navarro R, Ambrós S, Butković A *et al*. Defects in plant immunity modulate the rates and patterns of RNA virus evolution. *Virus Evol* 2022;**8**:veac059.

Nicaise V, Gallois J-L, Chafiai F *et al*. Coordinated and selective recruitment of eIF4E and eIF4G factors for potyvirus infection in *Arabidopsis thaliana*. *FEBS Lett* 2007;**581**:1041–46.

Pagán I, Alonso-Blanco C, García-Arenal F. The relationship of within-host multiplication and virulence in a plant-virus system. *PLoS One* 2007;**2**:e786.

Pagán I, García-Arenal F. Tolerance of plants to pathogens: an unifying view. *Annu Rev Phytopathol* 2020;**58**:77–96.

Pepin KM, Samuel MA, Wichman HA. Variable pleiotropic effects from mutations at the same locus hamper prediction of fitness from a fitness component. *Genetics* 2006;**172**:2047–56.

Peremyslov VV, Prokhnevsky AI, Avisar D *et al*. Two class XI myosins function in organelle trafficking and root hair development in Arabidopsis. *Plant Physiol* 2008;**146**:1109–16.

Pérez K, Yeam I, Kang B-C *et al*. Tobacco etch virus infectivity in *Capsicum* Spp. is determined by a maximum of three amino acids in the viral virulence determinant VPg. *Mol Plant-Microbe Interact* 2012;**25**:1562–73.

Phillips JC, Hardy DJ, Maia JDC *et al*. Scalable molecular dynamics on CPU and GPU architectures with NAMD. *J Chem Phys* 2020;**153**:044130.

Pichlmair A, Kandasamy K, Alvisi G *et al*. Viral immune modulators perturb the human molecular network by common and unique strategies. *Nature* 2012;**487**:486–90.

Rehman UU, Ghafoor D, Ullah A *et al*. Epigenetics regulation during virus-host interaction and their effects on the virus and host cell. *Microb Pathog* 2023;**182**:106271.

Roudet-Tavert G, Michon T, Walter J *et al*. Central domain of a potyvirus VPg is involved in the interaction with the host translation initiation factor eIF4E and the viral protein HCPro. *J Gen Virol* 2007;**88**:1029–33.

Rydzik AM, Warminski M, Sikorski PJ *et al*. mRNA cap analogues substituted in the tetraphosphate chain with CX2: identification of O-to-CCl2 as the first bridging modification that confers resistance to decapping without impairing translation. *Nucleic Acids Res* 2017;**45**:8661–75.

Sato M, Nakahara K, Yoshii M *et al*. Selective involvement of members of the eukaryotic initiation factor 4E family in the infection of *Arabidopsis thaliana* by potyviruses. *FEBS Lett* 2005;**579**: 1167–71.

Shearer HL, Cheng YT, Wang L *et al*. Arabidopsis clade I TGA transcription factors regulate plant defenses in an NPR1-independent fashion. *Mol Plant-Microbe Interact* 2012;**25**:1459–68.

Spivak M, Stone JE, Ribeiro J *et al*. VMD as a platform for interactive small molecule preparation and visualization in quantum and classical simulations. *J Chem Inf Model* 2023;**63**:4664–78.

Sun T, Busta L, Zhang Q *et al*. TGACG - BINDING FACTOR 1 (TGA 1) and TGA 4 regulate salicylic acid and pipecolic acid biosynthesis by modulating the expression of SYSTEMIC ACQUIRED RESISTANCE DEFICIENT 1 (*SARD 1*) *and CALMODULIN - BINDING PROTEIN 60g (CBP 60g)*. *New Phytol* 2018;**217**:344–54.

Svanella-Dumas L, Verdin E, Faure C *et al*. Adaptation of lettuce mosaic virus to *Catharanthus roseus* involves mutations in the central domain of the VPg. *Mol Plant-Microbe Interact* 2014;**27**: 491–97.

Szklarczyk D *et al*. The STRING database in 2023: protein-protein association networks and functional enrichment analyses for any sequenced genome of interest. *Nucleic Acids Res* 2023;**50**: gkac1000.

Tarazona A, Forment J, Elena SF. Identifying early warning signals for the sudden transition from mild to severe tobacco etch disease by dynamical network biomarkers. *Viruses* 2020;**12**:16.

Tisoncik-Go J, Gasper D, Kyle J *et al*. Integrated omics analysis of pathogenic host responses during pandemic H1N1 influenza virus infection: the crucial role of lipid metabolism. *Cell Host Microbe* 2016;**19**:254–66.

Truninger V, Aranda MA. Recessive resistance to plant viruses. *Adv Virus Res* 2009;**75**:119–59.

Uetz P, Dong Y-A, Zeretzke C *et al*. Herpesviral protein networks and their interaction with the human proteome. *Science* 2006;**311**:239–42.

Van Baalen M, Sabelis MW. The dynamics of multiple infection and the evolution of virulence. *Am. Nat*. 1995;**146**:881–910.

Van Zundert GCP, Rodrigues JPGLM, Trellet M *et al*. The HADDOCK2.2 web server: user-friendly integrative modeling of biomolecular complexes. *J Mol Biol* 2016;**428**:720–25.

Wan X, Yang T, Cuesta A *et al*. Discovery of lysine-targeted eIF4E inhibitors through covalent docking. *J Am Chem Soc* 2020;**142**:4960–64.

Wang C, Bradley P, Baker D. Protein-protein docking with backbone flexibility. *J Mol Biol* 2007;**373**:503–19.

Webb B, Sali A. Comparative protein structure modeling using MODELLER. *Curr Protoc Bioinf* 2016;**54**:5.6.1–37.

Wojcik R, Baranowski MR, Markiewicz L *et al*. Novel N7-arylmethyl substituted dinucleotide mrna 5′ cap analogs: synthesis and evaluation as modulators of translation. *Pharmaceutics* 2021;**13**:1941.

Zafirov D, Giovinazzo N, Lecampion C *et al*. Arabidopsis *eIF4E1* protects the translational machinery during TuMV infection and restricts virus accumulation. *PLoS Pathog* 2023;**19**: e1011417.

Zavaliev R, Dong X. NPR1, a key immune regulator of plant survival under biotic and abiotic stresses. *Molecular Cell* 2023;**84**: 131–41.

Virus Evolution, 2024, 10(1), veae055 , DOI: https://doi.org/10.1093/ve/veae055, Advance Access Publication 16 July 2024Research Article